

Article

Characterization and Luminescence of Eu^{3+} - and Gd^{3+} -Doped Hydroxyapatite $\text{Ca}_{10}(\text{PO}_4)_6(\text{OH})_2$

Veronica Paterlini ^{1,*},[†] , Marco Bettinelli ¹ , Rosanna Rizzi ², Asmaa El Khouri ³,
Manuela Rossi ⁴ , Giancarlo Della Ventura ⁵  and Francesco Capitelli ^{6,*} 

¹ Luminescent Materials Laboratory, Verona University, Ca' Vignal, Strada Le Grazie 15, 37134 Verona, Italy; marco.bettinelli@univr.it

² Institute of Crystallography–CNR, Via G. Amendola, 122/O, 70126 Bari, Italy; rosanna.rizzi@ic.cnr.it

³ Faculté des Sciences Semlalia, BP 2390, Université Cadi Ayyad, Marrakech 40000, Morocco; elkhouriasma@gmail.com

⁴ Department of Earth, Environmental and Resources Sciences, Federico II University, Via Cinthia 21, 80126 Naples, Italy; manuela.rossi@unina.it

⁵ Department of Science, Roma Tre University, Largo S. L. Murialdo 1, 00146 Rome, Italy; giancarlo.dellaventura@uniroma3.it

⁶ Institute of Crystallography–CNR, Via Salaria Km 29.300, 00016 Monterotondo (Rome), Italy

* Correspondence: veronica.paterlini@univr.it (V.P.); francesco.capitelli@ic.cnr.it (F.C.); Tel.: +39-045-802-7902 (V.P.); +39-069-067-2616 (F.C.)

† Present address: Department of Materials and Environmental Chemistry, Stockholm University, 106 91 Stockholm, Sweden.

Received: 21 August 2020; Accepted: 9 September 2020; Published: 11 September 2020



Abstract: Luminescence properties of europium-doped $\text{Ca}_{10-x}\text{Eu}_x(\text{PO}_4)_6(\text{OH})_2$ ($x_{\text{Eu}} = 0, 0.01, 0.02, 0.10$ and 0.20) and gadolinium-doped hydroxyapatite $\text{Ca}_{9.80}\text{Gd}_{0.20}(\text{PO}_4)_6(\text{OH})_2$ (HA), synthesized via solid-state reaction at $T = 1300$ °C, were investigated using scanning electron microscopy (SEM), powder X-ray diffraction (PXRD), Fourier transform infrared (FTIR), and luminescence spectroscopy. Crystal structure characterization (from unit cell parameters determination to refined atomic positions) was achieved in the $P6_3/m$ space group. FTIR analyses show only slight band shifts of (PO_4) modes as a function of the rare earth concentration. Structural refinement, achieved via the Rietveld method, and luminescence spectroscopy highlighted the presence of dopant at the Ca2 site. Strong luminescence was observed for all Eu- and Gd-doped samples. Our multi-methodological study confirms that rare-earth (RE)-doped synthetic hydroxyapatites are promising materials for bio-imaging applications.

Keywords: hydroxyapatite; rare earths; SEM; PXRD; FTIR; luminescence spectroscopy

1. Introduction

Synthetic hydroxyapatite $\text{Ca}_{10}(\text{PO}_4)_6(\text{OH})_2$ (HA) is the calcium phosphate compound having the most close affinities with the mineral component of human bones and teeth, with excellent biocompatibility and bioactivity, due to its non-toxic and noninflammatory properties [1]. For these reasons, the most common applications of HA are in biomedical sciences, although a wide range of other applications, e.g., as material suitable for laser ablation [2], host for toxic substances [3], and gas sensors [4] have been explored.

Specifically, in biomedical sciences, HA is used in: orthopedics, such as coating for metallic prosthesis, bone filler [5] and as composite materials HA/poly (L-lactide) for bone tissue scaffolds [6]; orthodontics, e.g., cements and dental implants [7]; oncology (cancer treatments) [8]; carrier in drug delivery applications [9,10], and so on. In this context, in recent years there has been a growing

interest in rare-earth (RE) doped HA materials, due to the excellent luminescence properties of RE, which has induced a strong interest in these materials for applications exploiting light-emission properties [11,12]. These materials are more suitable than the common fluorescent organic molecules, since their luminescence properties are not affected by the exposure to irradiation [10]. Moreover, incorporation of RE into the HA matrix overcomes the risk of toxicity deriving from RE ions in view of biomedical applications [13].

As a consequence, HA doped with RE ions is employed as cell labelling materials, owing to the strong luminescence under visible radiation, or as fluorescent probe, largely used for nondestructive observations both *in vivo* and *in vitro* [14]. The performance of the probe, in terms of luminescence intensity, typically depends on the crystallinity and crystal structure of the host material, and on the concentration of the RE used as dopant [14]. For these applications, the crystal chemical flexibility of HA allows the substitutions of many RE ions without any major modification at the two Ca1 and Ca2 sites; this feature has been also observed for all the most common $\text{Ca}_{10}(\text{PO}_4)_6(\text{F},\text{OH},\text{Cl})_2$ apatite species [15]. This property is mainly due to the ionic radii similarity between Ca^{2+} and RE^{3+} [16] allowing their easy exchange in the structure.

Among all RE-doped hydroxyapatites, europium-doped HA revealed to be an interesting luminescent material, due to Eu^{3+} ion's nondegenerate ground ($^7\text{F}_0$) and emitting ($^5\text{D}_0$) states, giving rise to luminescence spectra that provide valuable information about the local structure around the impurity ion [17]. As a consequence, there has been, in recent years, the production of a large number of Eu-HA systems employed as luminescent biomaterials [18–20]. We also point out that gadolinium-doped HA has been revealed to be a suitable species for bioimaging applications [21–23], due to its magnetic properties, while its luminescence efficiency upon gamma ray radiation can in turn be useful for dosimetry devices [23]. In particular, its emission in the UV range can be used as sensitizer in co-doped systems [13,22], but applications in many other fields such as phosphor [24] or antibacterial materials [25] can also be interesting.

In this work, we investigate the luminescence behaviour of a set of Eu^{3+} -doped $\text{Ca}_{10-x}\text{RE}_x(\text{PO}_4)_6(\text{OH})_2$ hydroxyapatite, with $x = 0, 0.01, 0.02, 0.10$ and 0.20 , and of $\text{Ca}_{9.80}\text{Gd}_{0.20}(\text{PO}_4)_6(\text{OH})_2$, through a multidisciplinary study based on scanning electron microscopy (SEM), powder X-Ray diffraction (PXRD), Fourier transform infrared (FTIR), and luminescence spectroscopies. This work is part of our ongoing investigation into the crystal chemistry and physical-chemistry of synthetic calcium phosphate materials [26–30]. The more profound investigation of the luminescence behavior of HA-Eu with respect to previous work concerning the luminescence of Eu^{3+} ion in HA-based materials is worth noting in the present work; this was accomplished by collecting well resolved spectra and lifetimes decays; in addition, the emission of Gd^{3+} ion in the compound $\text{Ca}_{9.80}\text{Gd}_{0.20}(\text{PO}_4)_6(\text{OH})_2$ was investigated for the first time. In both cases, luminescence features were related to their structure. Moreover, the structural analysis was improved by means of the Rietveld method.

2. Materials and Methods

The $\text{Ca}_{10-x}\text{RE}_x(\text{PO}_4)_6(\text{OH})_2$ samples under investigation in this study are labelled in the following way: HA = undoped hydroxyapatite, HA-Eu1 to HA-Eu4 = Eu-doped hydroxyapatite with $x_{\text{Eu}} = 0.01, 0.02, 0.10$ and 0.20 , respectively, while HA-Gd = Gd-doped hydroxyapatite with $x_{\text{Gd}} = 0.20$. Gd-doped HA with $x_{\text{Gd}} = 0.01, 0.02, 0.10$ were also preliminary investigated with luminescence spectroscopy; since they did not show any appreciable luminescence, they were not considered for the present study. X-ray structures were refined only for HA-Gd and HA-Eu compounds at higher concentrations (i.e., samples HA-Gd and HA-Eu4), to examine the site preference for the RE substituting for Ca.

The HA-RE samples were synthesized by the solid-state route. Stoichiometric amounts of CaCO_3 , CaHPO_4 , and RE_2O_3 (RE = Eu, Gd) were mixed using an agate mortar for 1 h. The homogenized powders were then placed in alumina crucibles and calcinated at high temperature ($T = 1300\text{ }^\circ\text{C}$) for 7 h [31].

Morphological analyses of the HA-RE samples were obtained by using a scanning electron microscope (SEM) JEOL-JSM 5310 (JEOL LTD, Tokio, Japan).

Powder XRD data of HA-Eu4 and HA-Gd samples were collected for structural analysis by using an automated Rigaku RINT2500 laboratory diffractometer (Rigaku Co., Tokio, Japan). Working at room temperature at 50 kV and 200 mA in Debye Scherrer geometry, the equipment uses an asymmetric Johansson Ge (111) crystal to select the monochromatic Cu $K\alpha_1$ radiation ($\lambda = 1.54056 \text{ \AA}$) and the silicon strip Rigaku D/teX Ultra detector (Rigaku Co., Tokio, Japan).

The 2θ angular range $10\text{--}120^\circ$ was scanned with a step size of 0.02° (2θ) and counting time of 4 s/step, by introducing the sample in a special glass capillary of 0.5 mm of diameter and mounted on the axis of the goniometer. To reduce the effect of possible preferred orientation, the capillary was rotated during measurement to improve the randomization of the orientations of the individual crystallites. The main acquisition parameters are reported in Table 1. All the powder structure solution steps: unit cell parameters calculation, identification of the space group, structure solution in reciprocal or direct space, and model refinement via the Rietveld method [32], were carried out by EXPO 2013 software [33].

Table 1. Main acquisition and structure refinement parameters for Eu-doped hydroxyapatite $\text{Ca}_{10}(\text{PO}_4)_6(\text{OH})_2$ (HA-Eu4) and Gd-doped hydroxyapatite $\text{Ca}_{10}(\text{PO}_4)_6(\text{OH})_2$ (HA-Gd) samples. FMLQ = full matrix least squares; Pearson VII [33].

Crystal Formula	HA-Eu4	HA-Gd
Refined formula	$(\text{Ca}_{4.88}\text{Eu}_{0.09})_2(\text{PO}_4)_6(\text{OH})_2$	$(\text{Ca}_{4.87}\text{Gd}_{0.11})_2(\text{PO}_4)_6(\text{OH})_2$
Formula weight	1019.50	1024.20
Color	Colorless	colorless
Temperature (K)	293	293
Wavelength (\AA)	1.54056	1.54056
2θ range; step ($^\circ$)	10-120, 0.02	10-120, 0.02
System, space group	Hex., $P6_3/m$	Hex., $P6_3/m$
$a = b$ (\AA)	9.41264(5)	9.41284(6)
c (\AA)	6.88038(..)	6.88151(10)
V (\AA^3)	527.917(3)	528.026(9)
Z; Density _{calc.} ($\text{Mg}\cdot\text{m}^{-3}$)	1, 3.207	1, 3.221
Refinement method	FMLQ	FMLQ
Bragg refl., parameters	879, 128	879, 128
R_p ; R_{wp} ; R_{exp} (%)	4.34, 5.80, 4.87	7.00, 9.31, 5.33

FTIR powder samples spectra were collected using a Nicolet iS50 FTIR spectrometer equipped (Thermo Fischer Scientific, Waltham, MA, USA) with a deuterated triglycine sulfate (DTGS) detector and a KBr beam splitter; the nominal resolution was 4 cm^{-1} and 64 scans were averaged for both sample and background. All samples were prepared as a KBr disk by mixing 1 mg of sample with 150 mg of KBr.

Room temperature luminescence spectra and decay curves were achieved by using a Fluorolog 3 (Horiba-Jobin Yvon) spectrofluorometer (Horiba Ltd., Kyoto, Japan), equipped with a Xe lamp, a double excitation monochromator, a single emission monochromator (Horiba Ltd., Kyoto, Japan) (mod. HR320) and a photomultiplier in photon counting mode for the detection of the emitted signal. The following set up was employed in order to obtain well resolved emission spectra: excitation at 393 nm; integration time: 0.5 s; slits: 5 (in)-2 (out) nm, filter 550 nm, step 0.2 nm. Integration time for HA-Eu4 was lowered to 0.2 s in order to avoid signal saturation. Lifetimes were measured using time-correlated single-photon counting technique (TCSPC), with a xenon microsecond pulsed lamp as excitation source. The decays curves were fitted by the Horiba Jobin Yvon DAS6 instrument software [34].

3. Results and Discussion

3.1. SEM Analysis

High-resolution SEM investigation of Eu-doped HA samples showed the presence of three different morphologies: compact and porous aggregates (Figure 1b,d,f,h), and massive fragments (Figure 1h). The porous aggregates are the most common, with the largest crystallite size of $\sim 10\ \mu\text{m}$ (Figure 1a,c,g). The massive fragments and compact aggregates have the largest dimension $\sim 35\ \mu\text{m}$ (Figure 1c,e,f) and $\sim 5\ \mu\text{m}$ (Figure 1e), respectively. In all cases, the crystallites show a rounded morphology, from elongated to sub-spherical, and the most common dimension is $\sim 5\ \mu\text{m}$. SEM investigations also suggested the growth of porous morphologies on massive fragments (Figure 1d,f,h).

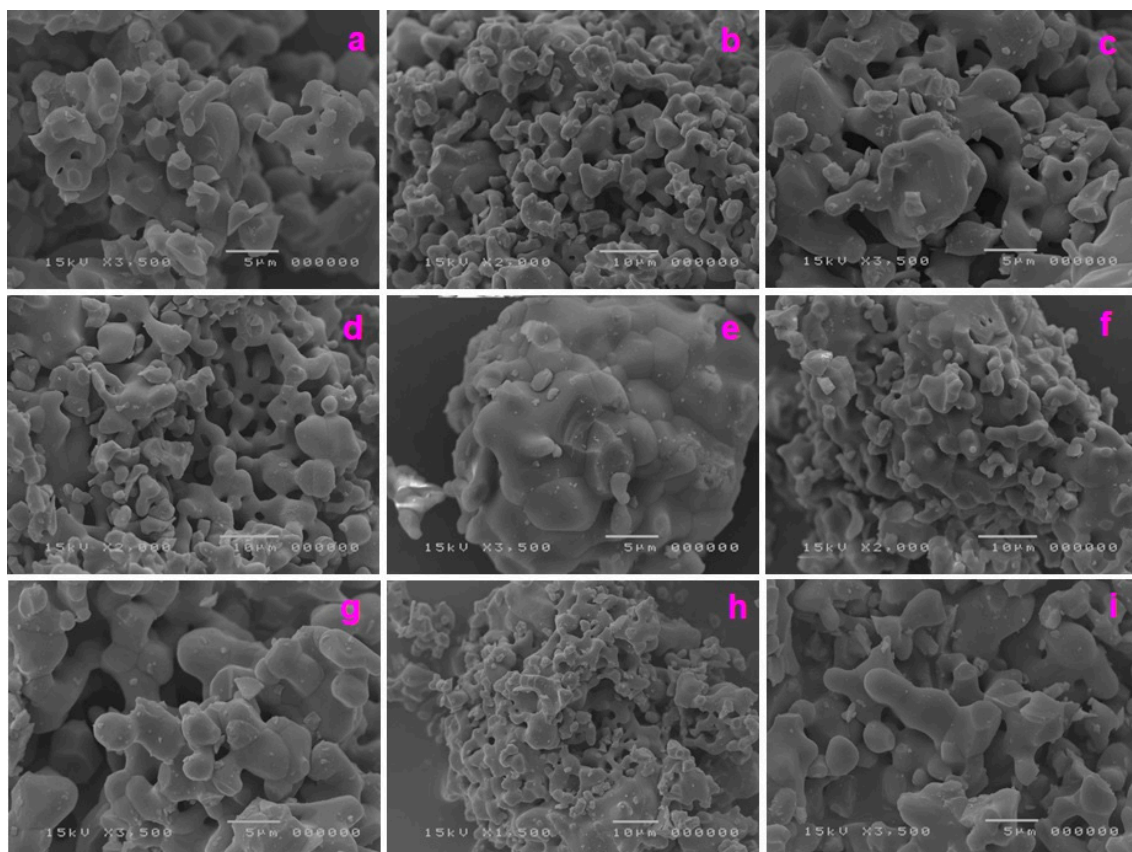


Figure 1. Scanning electron microscopy (SEM) images of Eu- and Gd-doped HA samples synthesized here. Detail of: HA-Eu1 at $5\ \mu\text{m}$ (a) and $10\ \mu\text{m}$ (b); HA-Eu2 at $5\ \mu\text{m}$ (c) and $10\ \mu\text{m}$ (d); HA-Eu3 at $5\ \mu\text{m}$ (e) and $10\ \mu\text{m}$ (f); HA-Eu4 at $5\ \mu\text{m}$ (g) and $10\ \mu\text{m}$ (h); HA-Gd at $5\ \mu\text{m}$ (i).

The shapes of Eu-doped HA crystallites synthesized in this study are similar to those described by [35], for the sample with Eu/Ca molar ratios of 7.5%, in [36], and by [37] (for the sample prepared at $\text{pH} = 12$). According to these papers, the spherical morphologies of the crystallites (phosphors) are ideal for enhancing brightness and resolution via the high packing density and the reduction of light scattering. This offers the possibility of brighter photoluminescence (PL) performance, higher definition, and improved screen packing [35,36]. This aspect is well-described by [35] that showed how the peak intensity of the PL spectra reached the maximum value for HA doped with 7.5 wt% of Eu^{3+} , and consisting of crystallites having clearly sub-spherical shapes.

The morphologies of the synthetic samples obtained in this work show some correlations with those described for Eu- and Gd-doped tricalcium phosphates by [27]. For example, the porous aggregates are very similar to microcrystalline aggregates found in $\text{Ca}_9\text{RE}(\text{PO}_4)_7$ ($\text{RE} = \text{Eu}$ and Gd),

in terms of dimension and microcrystals shape, even if in the doped HA samples, the porosity of aggregates are higher.

SEM analyses of sample HA-Gd showed the presence of porous aggregates composed by elongated and rounded crystallites with an average size of 5 μm (Figure 1i). These type of compounds were not so exhaustively studied from the morphological point of view as the analogue Eu phases, therefore there is scarce information in the literature. We can only quote the work of [37], where Gd-HA nanoparticles of $\sim 70 \mu\text{m}$ size were described, with a rounded morphology similar to the one observed in our HA-Gd synthetic product.

3.2. X-ray Structural Study

The crystal structure investigation was performed for Eu and Gd doped HA at highest concentration ($x = 0.2$), by using the EXPO software [33]. The indexing of the powder diffraction patterns by N-TREOR09 program [38], as integrated in EXPO, revealed a hexagonal unit cell typical of HA, with some unindexed diffraction peaks attributed to $\text{Ca}_3(\text{PO}_4)_3$ tricalcium phosphate (TCP) phase. The mixture is in agreement with [39] reporting a partial dissociation of HA into TCP at about 900 $^\circ\text{C}$.

The crystallinity of both HA-Eu4 and HA-Gd samples, calculated according to [40] was 97.07% and 99.03%, respectively, in agreement with the typical results for HA obtained from solid state synthesis [41,42].

The next step of the structure investigation revealed the hexagonal $P6_3/m$ space group for the hydroxyapatite [43], while the structure solution was obtained via the direct methods procedure in EXPO, confirming the hexagonal $P6_3/m$ model reported in [43]. The obtained structure was submitted to structural refinement by the Rietveld method, assuming both calcium sites as possible localizations of the dopant rare earth. Detailed crystallographic results are given in Table 1. The following refinement strategy was applied: in the sites shared by Ca and rare earth, the position and the thermal parameter of both occupants were constrained to be equal, and the sum of Ca and RE occupancies fixed according to the experimental crystal chemical formulas. Moreover, the thermal parameters of P and O atoms were constrained to be equal. Hydrogen atoms were not found by Fourier analysis. The main crystal structure refinements data are reported in Table 1. The agreement between the observed (blue line) and the calculated (red line) diffraction pattern is displayed, together with the background (green line) and the difference pattern plotted on the same scale (violet line), in Figure 2a,b for HA-Eu4 and HA-Gd samples, respectively.

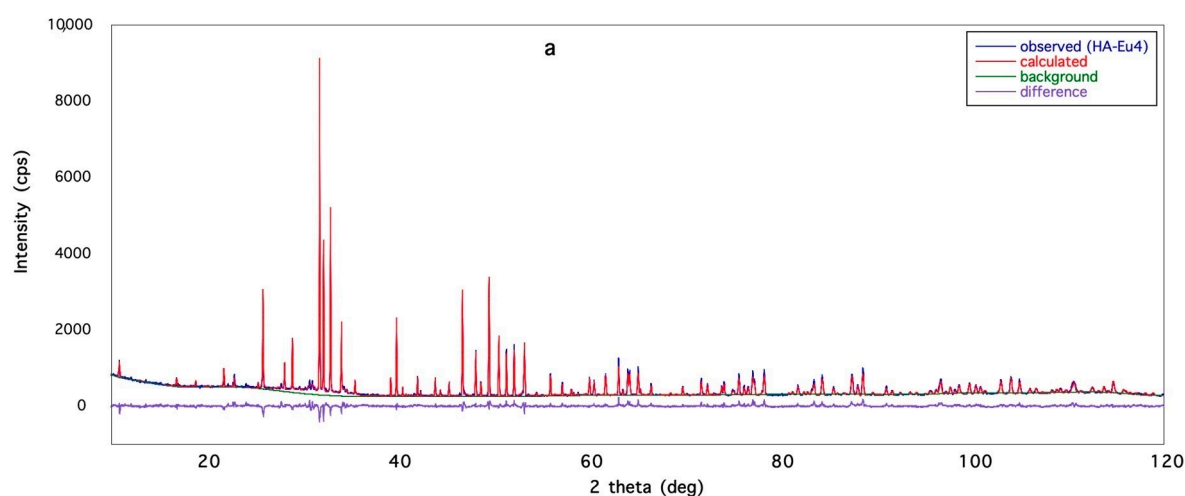


Figure 2. Cont.

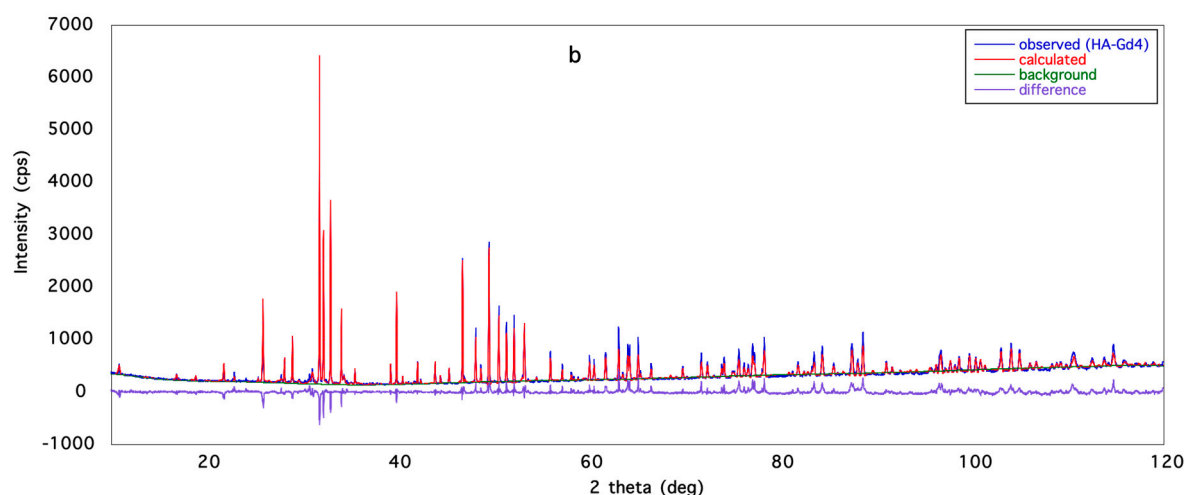


Figure 2. Rietveld plots of HA-Eu4 (a) and HA-Gd (b) samples. Observed diffraction profile (blue line), calculated profile (red line), background (green line) and difference profile (violet line).

Table 2. the P site being a quite regular tetrahedron (Figure 3), with bond lengths in the range 1.530(6)–1.566(5) Å for HA-Eu4, and 1.562(14)–1.599(7) Å for HA-Gd (Table 3).

Table 2. Atomic position, isotropic thermal parameters, and site occupancy for HA-Eu4 and HA-Gd samples.

Atom	Site	<i>x</i>	<i>y</i>	<i>z</i>	U_{eq}	Occ.
HA-Eu4						
Ca1	4 <i>f</i>	2/3	1/3	−0.0016(5)	0	1
Ca2	6 <i>h</i>	1.0073(3)	0.2513(2)	1/4	0	0.961(1)
Eu1	6 <i>h</i>	1.0073(3)	0.2513(2)	1/4	0.0000(3)	0.029(1)
P1	6 <i>h</i>	1.0291(3)	0.3978(3)	−1/4	0.0012	1
O1	6 <i>h</i>	0.8430(6)	0.3261(6)	−1/4	0.0012	1
O2	6 <i>h</i>	0.8773(7)	0.4111(7)	1/4	0.0001	1
O3	12 <i>i</i>	1.0854(5)	0.3385(5)	−0.0682(6)	0.0112	1
O4	4 <i>e</i>	0	0	0.2000(18)	0.0156(5)	0.5
HA-Gd						
Ca1	4 <i>f</i>	2/3	1/3	−0.0004(8)	0	1
Ca2	6 <i>h</i>	1.0076(4)	0.2518(4)	1/4	0	0.956(2)
Gd1	6 <i>h</i>	1.0076(4)	0.2518(4)	1/4	0.0000(6)	0.034(2)
P1	6 <i>h</i>	1.0309(6)	0.3990(5)	−1/4	0.0035	1
O1	6 <i>h</i>	0.8407(11)	0.3240(11)	−1/4	0	1
O2	6 <i>h</i>	0.8788(12)	0.4086(12)	1/4	0.0096	1
O3	12 <i>i</i>	1.0869(8)	0.3367(8)	−0.0647(9)	0.0035	1
O4	4 <i>e</i>	0	0	0.197(3)	0.0035(8)	0.5

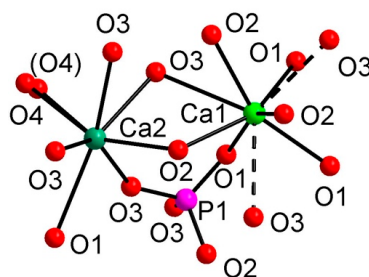


Figure 3. Coordination environments around the Ca1 and Ca2 sites in hydroxyapatite. Dashed lines: Ca-O interactions >2.8 Å.

Table 3. Bond distances (Å) and bond valence parameters (valence units) for HA-Eu4 and HA-Gd samples. The Ca2-O values are calculated taking into account the refined occupancy parameters for Ca and Eu (Table 2).

Distance	HA-Eu4	bvp	HA-Gd	bvp
3xCa1-O1	2.406(5)	0.30	2.404(8)	0.31
3xCa1-O2	2.452(5)	0.27	2.459(9)	0.26
3xCa1-O3	2.830(4)	0.10	2.833(7)	0.10
Ca2-O1	2.687(5)	0.14	2.670(13)	0.15
Ca2-O2	2.367(9)	0.34	2.332(5)	0.37
2xCa2 O3	2.325(4)	0.38	2.300(6)	0.41
2xCa2 O3	2.486(4)	0.25	2.479(9)	0.25
Ca2-O _{4H}	2.357(3)	0.35	2.364(5)	0.34
P1-O1	1.530(6)	1.26	1.562(14)	1.16
P1-O2	1.558(6)	1.17	1.569(10)	1.14
2xP1-O3	1.566(5)	1.15	1.599(7)	1.05

The Ca atoms are engaged in complex co-ordinations: Ca1 in a CaO₉ polyhedron (Figure 3), with three couples of bond distances related by symmetry, ranging from 2.406(5)–2.830(4) Å for HA-Eu4, and 2.404(8)–2.833(7) Å for HA-Gd (Table 3). The Ca1-O3 distance slightly exceeds the bonding sphere of Ca, providing a weak contribution to the bond valence [44] to Ca1, as discussed later (see also Table 3). Actually, based on the refined distances, we could describe the Ca1 site as a CaO₆ polyhedron, the Ca1...O3 being interpreted as relatively weak interactions. The Ca2 polyhedron displays a CaO₆(OH) coordination, resembling a distorted pentagonal bipyramid with five bonds (1xCa2-O1 and two couples of symmetry-related Ca2-O3 bonds) on the equatorial plane, and vertices consisting of one O2 atom and one OH group. The Ca2-O distances are in the range 2.325(4)–2.687(5) Å (HA-Eu4), and 2.300(10)–2.670(13) Å (HA-Gd).

For both compounds, all P-O and Ca-O bond distances are in good agreement with those observed in other HA structural investigations [45].

As observed in the work of Rossi et al. [46], the O4 hydroxyl atoms occupy the 4e sites, split above or below the mirror planes, with a disordered site-distribution (Table 2). This arrangement causes a local deviation from the P₆₃/m symmetry, with a consequent lack of the mirror plane, being only one of the two mirror-related sites statistically occupied. However, because each mirror-related site is half occupied, the average P₆₃/m symmetry is preserved [15].

To support the Rietveld refinement results for the distribution of RE dopants within the available sites, we examined the calculated bond valence parameters [44], testing the possible dopant localization at both Ca1 and Ca2 cationic positions: the occupancy refinements unambiguously converged into the presence of the rare earth cation at the Ca2 site for both samples (Table 2), in agreement with the substitution mechanisms described by Fleet et al. [47] and by Graeve et al. [48]. This conclusion was confirmed by the calculated excess charge converging to the Ca2 position, resulting in 2.09 v.u. for HA-Eu4 and 2.18 v.u. for HA-Gd, while Ca1 displayed values close to the ideal charge of 2.00 for both phases. For packing reasons, and to balance the excess charge at Ca2, the P site resulted under-bonded in both structures, with 4.73 v.u. and 4.40 v.u. for HA-Eu4 and HA-Gd, respectively. The final results of bond valence parameters analysis are given in Table 3.

Hexagonal P₆₃/m hydroxyapatite, whose crystal formula can be written as [Ca₁₄Ca₂](PO₄)₆(OH)₂, shows a zeolitic character; it can be described as a framework of columns of face-sharing Ca₁₀O₆ metaprisms (a polyhedron intermediate between an octahedron and a trigonal prism), corner-connected to PO₄ tetrahedra down [001]; such an arrangement indeed creates one-dimensional tunnels occupied by [Ca(2)₆(OH)₂]¹⁰⁺ counter-ions (Figure 4). The Ca₁₀O₆ metaprism is ideally built up by the six strongest Ca-O bond distances; those over 2.8 Å are not considered. The HA framework has the ideal stoichiometry [Ca₁₄(PO₄)₆]¹⁰⁻, with the hexagonal channel containing [Ca₂₆(OH)₂]¹⁰⁺ moieties acting as counter-ions [49], while the Ca1-O3 interactions further stabilize the framework.

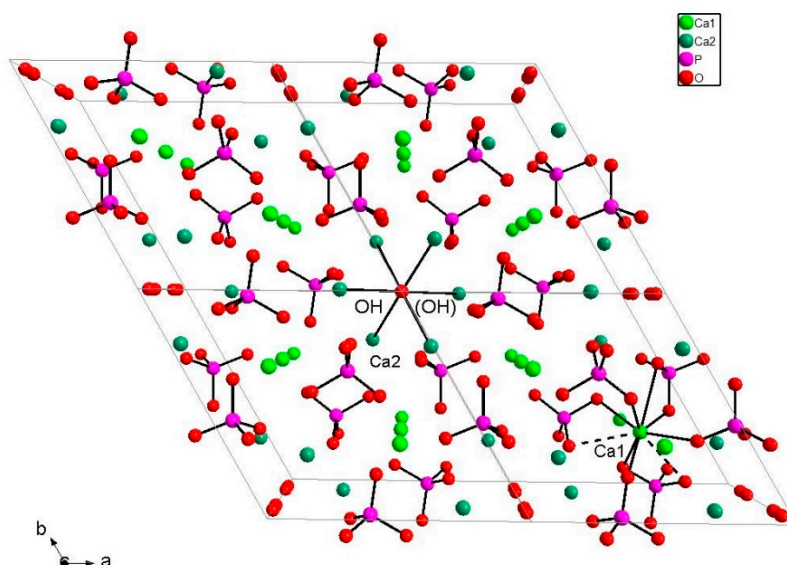


Figure 4. Three-dimensional framework of HA-Eu4 sample, showing details of Ca_1O_6 metaprisms, and $\text{Ca}_2_6(\text{OH})_2$ groups. The OH groups correspond to O4 atoms. Ca1-O3 bonds are dashed for clarity.

3.3. FTIR Spectroscopy

The powder FTIR absorbance spectra of HA-Eu and HA-Gd samples were collected in the $400\text{--}4000\text{ cm}^{-1}$ wavenumber range and are shown in Figure 5, in comparison with the pattern of undoped HA. Measured band positions (wavenumbers, cm^{-1}) are listed in Table 4.

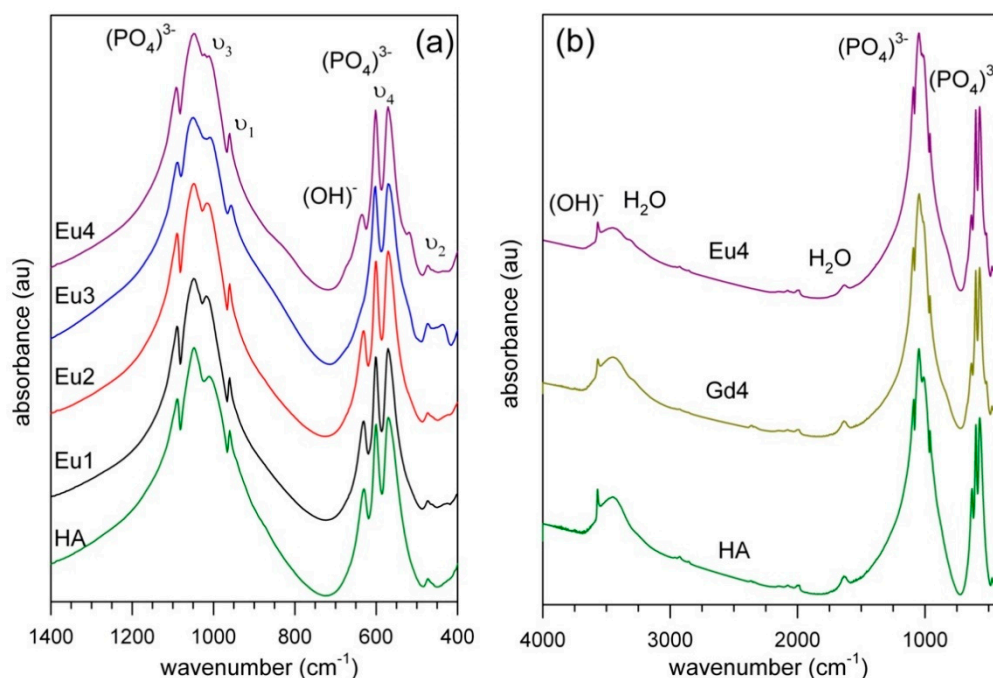


Figure 5. (a) Fourier transform infrared (FTIR) spectra of Eu-doped HA samples in comparison with undoped HA in the low-frequency ($<1200\text{ cm}^{-1}$) lattice mode region; (b) comparison between the spectra of samples HA-Gd and HA-Eu4 in the full range $4000\text{--}400\text{ cm}^{-1}$.

Table 4. Measured absorption features in the FTIR spectra and relative assignments for HA samples.

HA	HA-Eu1	HA-Eu2	HA-Eu3	HA-Eu4	HA-Gd	Assignment
3569	3570	3569	3566	3569	3569	$\nu_s(\text{OH})$
1633	1633	1634	1633	1633	1633	$\delta(\text{H}_2\text{O})$
1090	1090	1090	1090	1091	1091	
1047	1047	1047	1047	1048	1048	$\nu_3(\text{PO}_4)^{3-}$
1015	1015	1015	1015	1015	1015	
960	960	960	960	961	961	$\nu_1(\text{PO}_4)^{3-}$
633	633	633	-	632	632	$\nu_1(\text{OH})$
600	600	600	601	602	602	
574	570	570	570	571	571	$\nu_4(\text{PO}_4)^{3-}$
-	-	-	-	518	518	RE-O
472	472	472	472	473	473	$\nu_2(\text{PO}_4)^{3-}$

Interpretation of the spectra can be based on the vast literature for phosphate compounds [50–55]. Accordingly, in the higher wavenumber 4000–3000 cm^{-1} range the well resolved and relatively sharp peak at 3570 cm^{-1} is assigned to the $(\text{OH})^-$ stretching mode [56]. This peak is superimposed to a broad absorption extending from 3600 to 3000 cm^{-1} that is due to H_2O (moisture) adsorbed on the KBr disk [57]. The bending mode of these moisture molecules occurs around 1600 cm^{-1} (Figure 5b).

In the lower wavenumber region, the most intense peaks in the 1090–1000 cm^{-1} range can be assigned to the triply degenerated antisymmetric stretching modes (ν_3) of the phosphate group $(\text{PO}_4)^{3-}$ [58], while the medium-intense peak at 960 cm^{-1} is due to the symmetric stretching of this anion. Two medium intense and very sharp peaks at 602 and 564 cm^{-1} can be related to the triple degenerate antisymmetric bending mode of the $[\text{PO}_4]^{3-}$ group [14]. Analysis of deuterated samples [56] shows that the relatively sharp peak at 663 cm^{-1} is due to the O-H libration. According to [59], the sharpness of selected bands in the phosphate region, especially 632 cm^{-1} , 602 cm^{-1} , and 564 cm^{-1} , are an experimental indication of good crystallinity of the hydroxyapatite, confirming the XRD results. Finally, the band at 475 cm^{-1} can be attributed to the $\nu_2(\text{PO}_4)^{3-}$ mode [60]. It is worth noting that the presence, in samples with the higher concentration of dopant, of a peak at 518 cm^{-1} that could be assigned to the RE-O mode as proposed by for La and by [58], for Gd-doped hydroxyapatites prepared at high annealing temperatures. Last, in HA-Eu3 sample, the weak peak at 460 cm^{-1} is attributed to trace amounts of $\text{Ca}_3(\text{PO}_4)_2$ (TCP) that are occasionally associated with hydroxyapatite synthesized at high temperature [30].

For increasing concentration of the RE dopant no significant modifications of the spectra (Figure 5), except slight peak shift, are observed (Table 4).

3.4. Luminescence Spectroscopy

3.4.1. Eu^{3+} Dopant

The analysis of the luminescence revealed significant emission bands for all Eu-doped HA samples, and for the Gd-doped sample. It should be pointed out that while Eu^{3+} luminescence was clearly observed at all investigated concentrations, for Gd^{3+} only the highest concentration (2%) yielded an observable emission. At lower doping amounts, the intensity was too weak, thus all other samples with lower gadolinium concentrations were abandoned for the present study.

The room temperature excitation and emission spectra collected for the representative HA-Eu4 sample are displayed in Figure 6a,b, respectively.

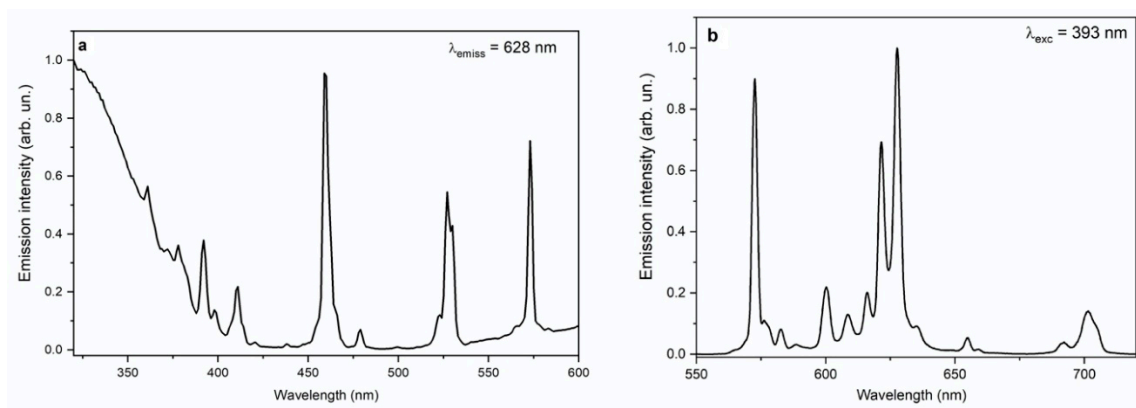


Figure 6. (a) Normalized excitation spectrum of HA-Eu4, detecting the emission at 628 nm. (b) Emission spectrum of HA-Eu4, collected upon excitation at 393 nm.

The most striking feature that is worth noting, however, is the strong intensity of the emission peak at 573 nm that corresponds to the ${}^5D_0 \rightarrow {}^7F_0$ forbidden transition of Eu^{3+} . This band acquires intensity only in the presence of a strong covalent bond involving the impurity ion [61,62]. This unusual behavior is addressed below. The profile of the ${}^5D_0 \rightarrow {}^7F_0$ band for the present samples is Gaussian, with a full width at half maximum (FWHM) around 70 cm^{-1} , which is a high value for a crystalline material, and comparable with the one typically observed in glasses [63]. This observation is therefore compatible with the accommodation of Eu^{3+} in a distribution of sites affected by the presence of significant disorder.

Inspection of the excitation spectra obtained at the 628 nm emission line (Figure 6a), shows that the most intense excitation peak is at 460 nm, corresponding to the ${}^7F_0 \rightarrow {}^5D_2$ transition. In addition, a broad band occurs in the 260–350 nm range, that is due to $\text{Eu}^{3+}\text{-O}^{2-}$ charge transfer (CT band).

Decay curves were collected at room temperature in correspondence of maxima at 573 and 628 nm for all samples, upon excitation at 393 and 460 nm. Normalized decay curves obtained at $\lambda_{\text{exc}} = 393 \text{ nm}$ and $\lambda_{\text{emiss}} = 628 \text{ nm}$ are shown in Figure 7. In these conditions all the decay curves can be described by a single exponential. As a result, independently of the excitation wavelengths (in the range 320–530 nm) and of the Eu^{3+} concentration, the decay times measured at 573 and 628 nm are close to 0.45 ms. This decay time is shorter than the one normally observed for anhydrous materials ($\geq 1 \text{ ms}$) and is more typical of hydrated oxides.

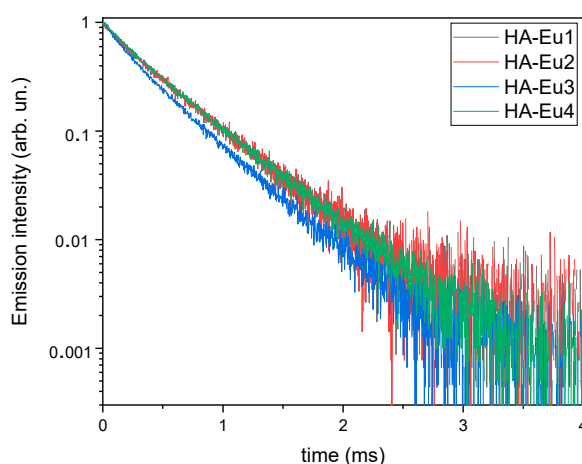


Figure 7. Normalized decay curves in correspondence of $\lambda_{\text{exc}} = 393 \text{ nm}$ and $\lambda_{\text{emiss}} = 628 \text{ nm}$.

As already pointed out, a remarkable feature of all HA-Eu doped samples is the strong intensity of the forbidden europium $^5D_0 \rightarrow ^7F_0$ transition. A similar behaviour was reported by [30,64] for samples treated at $T > 900^\circ$, while for samples synthesized at 600° the same forbidden transition was reported to occur with less intensity [30]. The examined structure is that of HA; above a certain concentration of RE dopant we observe the formation of additional phases in the assemblage. According to [65], Ca phosphate and Ca oxide occur in low concentrations until Eu reaches about 5%. $Ca_3(PO_4)_2$ tricalcium phosphate (TCP) begins to appear in the assemblage at 600° in the presence of Eu at 4% [64]. The complete transformation of HA into β -TCP is observed for $T > 1000^\circ$ for different thermal treatments [48]. Moreover, the presence of Eu^{3+} ions has been shown to inhibit the crystallization of nano-sized HA [64]. The loss of OH^- group for higher T is also feasible to induce a local structural distortion [48], that probably involves the anomalous appearance of the forbidden transition. This feature is unusual and was previously found in similar nano crystalline $Ca_{10}(PO_4)_6(OH)_2$ doped with 3% of Eu^{3+} [30], while the hypersensitive $^5D_0 \rightarrow ^7F_2$ transition was otherwise dominant in HA-Eu materials [6,10,13].

For samples whose spectra were obtained under experimental conditions allowing high spectral resolution (i.e., low temperature, laser excitation, etc.), the $^5D_0 \rightarrow ^7F_0$ transition shows a single band [66], indicating the disorder of Eu^{3+} at non-equivalent Ca^{2+} sites, i.e., Ca1 (higher symmetry) and Ca2 (lower symmetry). In particular, Eu^{3+} may enter preferentially the Ca2 site in order to better optimize the charge balance through the thermal diffusion mechanism occurring in these materials [10,66]. The mechanism can be described according to [64]



On the other hand another charge compensation mechanism is possible [64]:



implying the creation of Ca^{2+} vacancies.

In the present samples, the first mechanism (Equation (1)) is undoubtedly active, given the close similarity of the luminescence spectra to the ones reported by [67] for the Eu^{3+} in HA and oxyapatites, in particular for the unusually strong 0-0 transition [67]. The explanation of the abnormal intensity of the formally forbidden 0-0 transition was proposed on the basis of the strong covalence of the $Eu^{3+}-O^{2-}$ bond in the Ca2 sites [61,62,66,67]. However, the presence of a relatively short decay time of about 0.45 ms for the emission at 573 nm (corresponding to the 0-0 band) indicates that the 5D_0 level is also affected by multiphonon relaxation induced by the O-H vibrations (Equation (1)). It is worth to noting that the presence of vibronic sidebands ascribed to coupling between the Gd^{3+} and O-H vibrations indicate that a fraction of the RE impurities enter the HA lattice also through the mechanism presented in Equation (2) (see below). It is, however, plausible that traces of the dopant can be present in Ca1 sites even for higher synthesis temperature, although they are not directly detected in the present study by luminescence spectroscopy, while being invisible to a long-range technique like X-ray diffraction.

3.4.2. Gd^{3+} Dopant

The Gd-doped sample, HA-Gd showed strong UV luminescence. In fact, the bands are well resolved both in the excitation and in the emission spectra, displaying narrow peaks (Figure 8a), as it usual for 4f-4f transitions. However, this is the first time that the optical properties of Gd^{3+} are studied in relation to the HA structure.

Upon excitation in the 6I_J ($J = 7/2-17/2$) region, emission bands corresponding to $^6P_{5/2} \rightarrow ^8S_{7/2}$ and $^6P_{7/2} \rightarrow ^8S_{7/2}$ transitions are observed, with the stronger peak at 314 nm ($31,806 \text{ cm}^{-1}$) as observed for Gd^{3+} in different hosts [68–71], suitable for potential multimodal applications [23]. It is interesting to point out that weak, but clear vibronic bands are detected at 319.6, 325, and 351 nm in the emission spectrum, located respectively at energy differences from the purely electronic transition that

correspond to features present in the FTIR spectrum [72], as reported in Figure 8b. We note that similar sidebands are also observed in the excitation spectrum (not shown here for brevity).

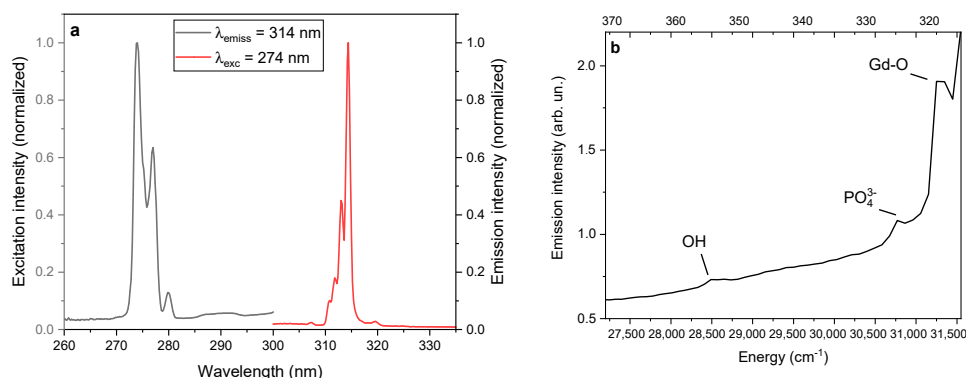


Figure 8. (a) HA-Gd excitation (detecting the emission at 314 nm) and emission (excitation at 274 nm) spectra; (b) vibronic bands and assignments in the HA-Gd emission spectrum.

The sharp purely electronic lines in the optical spectra of RE ions are often accompanied by other weak peaks, corresponding to the vibronic transitions [72]. The position and intensity of these transitions are strongly related to the surrounds of the ions, thus they can give information about the nature of the chemical environment and the vibrational coupling with the $4f^n$ electrons. [71,73]. For Gd^{3+} , the vibronic intensity are mainly due to vibronically-induced forced electric dipole transitions [71]. To the best of our knowledge, this is the first time that vibronic sidebands of this type have been observed in the case of Gd^{3+} present as impurity in HA.

The energy of the vibronic peaks observed in HA-Gd suggests that the electronic levels of the impurity ion are coupled to local Gd-O vibrations in the first coordination sphere, and to vibrations in more distant phosphate and hydroxyl molecular ions. Indeed, we observe an intensity ratio between the O-H vibronic peak and the main electronic transition ${}^6P_{7/2} \rightarrow {}^8S_{7/2}$ of about 3%, confirming the presence of coupling of the Gd^{3+} ion to this high energy vibration [68]. In turn, this observation proves that not only the charge compensation mechanism reported in Equation (1) (for Eu^{3+}) is present, but also the one presented in Equation (2). This should affect the non-radiative decay of the excited states of the impurity ions [68] (see below).

The excitation spectrum shows three main peaks in the region corresponding to ${}^8S_{7/2} \rightarrow {}^6I_{7/2}$ transition. The decay curve corresponding to the 314 nm emission peak, obtained upon pulsed 274 nm excitation, is characterized by an exponential profile with a decay time of 0.76 ms. This value is shorter than the typical decay times for the Gd^{3+} ion in phosphate hosts, which can be as long as 2.72 ms [73], so that non-radiative decay due to the interaction with O-H vibrations is likely to be operative. This results nicely agrees with the coupling of the Gd^{3+} ion with hydroxyl vibrations evidenced by the presence of relevant vibronic sidebands. In addition, it explains the short decay times observed for HA doped with Eu^{3+} (see above).

4. Conclusions

Luminescence properties of Eu-doped $Ca_{10-x}Eu_x(PO_4)_6(OH)_2$ ($x_{Eu} = 0, 0.01, 0.02, 0.10$ and 0.20) and Gd-doped $Ca_{9.80}Gd_{0.20}(PO_4)_6(OH)_2$ hydroxyapatite powder samples, synthesized via solid state reaction at $T = 1300$ °C, were fully characterized through a multi-methodological approach based on SEM microscopy, powder X-ray diffraction, FTIR, and luminescence spectroscopy. SEM analysis showed the presence of three different morphologies (compact, porous, and aggregates), with the most common average size being ~ 10 μm ; crystal structure refinement via the Rietveld method ($P6_3/m$ space group) showed how the RE ions are strongly ordered at the Ca2 site, a feature that is in agreement with the high temperature of synthesis; FTIR showed slight band shifts of modes typical of the (PO_4) moiety as a function of the rare earth concentration rate. Beside the strong luminescence observed for

all of the samples investigated, the Gd-doped hydroxyapatite also showed interesting vibronic features that revealed information about the electron-phonon coupling in the HA-doped host. The results obtained are in agreement with the presence of RE ions at the Ca2 site as refined based on the XRD data; the short decay times and the presence of vibronic sidebands assigned to the coupling with hydroxyl anions indicate that two charge compensation mechanisms are present. One of these implies the formation of free oxide ions, and the other the creation of Ca²⁺ vacancies. In conclusion, this work provides new insights into the luminescent properties and the local structure of hydroxyapatites doped with rare-earth ions and produced by high temperature synthesis. This information will be useful for the design of biocompatible synthetic materials for bio-imaging applications. This work also stresses the need for multi-methodological approaches for a full and detailed characterization of this class of materials.

Author Contributions: All the authors conceived and designed the main ideas together, supervised the whole work, and wrote the text; A.E.K. contributed in the synthesis; M.R. contributed in SEM-EDS analysis; R.R. and F.C. contributed in PXRD data collections and Rietveld refinements; G.D.V. contributed in FTIR spectroscopy; V.P. and M.B. contributed in luminescence spectroscopy. All authors have read and agreed to the published version of the manuscript.

Funding: This research received no external funding. G.D.V. was financially supported by MIUR-Italy Dipartimenti di Eccellenza, ARTICOLO 1, COMMI 314–337 LEGGE 232/2016.

Acknowledgments: Research developed within the activities of CNR (Italy)–CNRST (Morocco) bilateral project 2016–17 ‘Novel Ca₉RE(PO₄)₇ biomaterials: synthesis and multi-methodological characterization via X-ray techniques’ reference CNR 1588/16. The authors gratefully thank Erica Viviani (Verona University), Federico Galdenzi (Roma Tre University) and Francesco Baldassarre (IC-CNR) for expert technical assistance, and the Facility “Centro Piattaforme Tecnologiche” of the University of Verona for access to the Fluorolog 3 (Horiba-Jobin Yvon) spectrofluorometer. University of Verona is gratefully acknowledged.

Conflicts of Interest: The authors declare no conflict of interest. The founding sponsors had no role in the design of the study; in the collection, analyses, or interpretation of data; in the writing of the manuscript, and in the decision to publish the results.

References

1. Dorozhkin, S.V. Hydroxyapatite and other calcium orthophosphates: Bioceramics, coatings and dental applications. In *Hydroxyapatite and Other Calcium Orthophosphates: Bioceramics, Coatings and Dental Applications*; Nova Science Publishers: New York, NY, USA, 2017; pp. 1–462.
2. Martinez, M.; Bayne, C.; Aiello, D.; Julian, M.; Gaume, R.; Baudalet, M. Multi-elemental matrix-matched calcium hydroxyapatite reference materials for laser ablation: Evaluation on teeth by laser-induced breakdown spectroscopy. *Spectrochim. Acta Part B At. Spectrosc.* **2019**, *159*, 105650. [[CrossRef](#)]
3. Smičiklas, I.D.; Milonjić, S.K.; Pfendt, P.; Raičević, S. The point of zero charge and sorption of cadmium (II) and strontium (II) ions on synthetic hydroxyapatite. *Sep. Purif. Technol.* **2000**, *18*, 185–194. [[CrossRef](#)]
4. Khairnar, R.S.; Mene, R.U.; Munde, S.G.; Mahabole, M.P. Nano-hydroxyapatite thick film gas sensors. *AIP Conf. Proc.* **2011**, *1415*, 189–192.
5. Cardoso, G.B.C.; Tondon, A.; Maia, L.R.B.; Cunha, M.R.; Zavaglia, C.A.C.; Kaunas, R.R. In Vivo approach of calcium deficient hydroxyapatite filler as bone induction factor. *Mater. Sci. Eng. C* **2019**, *99*, 999–1006. [[CrossRef](#)] [[PubMed](#)]
6. Szyszka, K.; Targonska, S.; Gazinska, M.; Szustakiewicz, K.; Wiglusz, R.J. The comprehensive approach to preparation and investigation of the Eu³⁺ doped hydroxyapatite/poly(L-lactide) nanocomposites: Promising materials for theranostics application. *Nanomaterials* **2019**, *9*, 1146. [[CrossRef](#)]
7. Anita Lett, J.; Sundareswari, M.; Ravichandran, K. Porous hydroxyapatite scaffolds for orthopedic and dental applications—The role of binders. *Mater. Today Proc.* **2016**, *3*, 1672–1677. [[CrossRef](#)]
8. Kamitakahara, M.; Ohtoshi, N.; Kawashita, M.; Ioku, K. Spherical porous hydroxyapatite granules containing composites of magnetic and hydroxyapatite nanoparticles for the hyperthermia treatment of bone tumor. *J. Mater. Sci. Mater. Med.* **2016**, *27*, 93. [[CrossRef](#)]
9. Singh, G.; Singh, R.P.; Jolly, S.S. Customized hydroxyapatites for bone-tissue engineering and drug delivery applications: A review. *J. Sol-Gel Sci. Technol.* **2020**, *94*, 505–530. [[CrossRef](#)]

10. Zhang, C.; Uchikoshi, T.; Liu, L.; Cai, G.; Si, J.; Hirosaki, N. Synthesis of Eu-doped hydroxyapatite whiskers and fabrication of phosphor layer via electrophoretic deposition process. *J. Am. Ceram. Soc.* **2020**, in press.
11. Machado, T.R.; Sczancoski, J.C.; Beltrán-Mir, H.; Nogueira, I.C.; Li, M.S.; Andrés, J.; Cordoncillo, E.; Longo, E. A novel approach to obtain highly intense self-activated photoluminescence emissions in hydroxyapatite nanoparticles. *J. Solid State Chem.* **2017**, *249*, 64–69. [[CrossRef](#)]
12. Zhang, X.; Zhang, J.; Ma, W.; Liao, S.; Zhang, X.; Wang, Z.; Yu, L.; Lian, S. From Nonluminescence to Bright Blue Emission: Boron-Induced Highly Efficient Ce₃₊-Doped Hydroxyapatite Phosphor. *Inorg. Chem.* **2019**, *58*, 13481–13491. [[CrossRef](#)] [[PubMed](#)]
13. Mondal, S.; Nguyen, V.T.; Park, S.; Choi, J.; Vo, T.M.T.; Shin, J.H.; Kang, Y.-H.; Oh, J. Rare earth element doped hydroxyapatite luminescent bioceramics contrast agent for enhanced biomedical imaging and therapeutic applications. *Ceram. Int.* **2020**, in press. [[CrossRef](#)]
14. Iconaru, S.-L.; Motelica-Heino, M.; Predoi, D. Study on Europium-Doped Hydroxyapatite Nanoparticles by Fourier Transform Infrared Spectroscopy and Their Antimicrobial Properties. *J. Spectrosc.* **2013**, *2013*, 284285. [[CrossRef](#)]
15. Hughes, J.M.; Rakovan, J. The crystal structure of apatite, Ca₅(PO₄)₃(F,OH,Cl). *Phosphates Geochem. Geobiol. Mater. Importance* **2019**, *48*, 1–12.
16. Shannon, R.D. Revised effective ionic radii and systematic studies of interatomic distances in halides and chalcogenides. *Acta Crystallogr. A* **1976**, *32*, 751–767. [[CrossRef](#)]
17. Binnemans, K. Interpretation of europium (III) spectra. *Coord. Chem. Rev.* **2015**, *295*, 1–45. [[CrossRef](#)]
18. Vasugi, G.; Thamizhavel, A.; Girija, E.K. Luminescence studies of rare-earth doped and Co-doped hydroxyapatite. *AIP Conf. Proc.* **2012**, *1447*, 267–268.
19. Nikolaev, A.; Kolesnikov, I.; Frank-Kamenetskaya, O.; Kuz'mina, M. Europium concentration effect on characteristics and luminescent properties of hydroxyapatite nanocrystalline powders. *J. Mol. Struct.* **2017**, *1149*, 323–331. [[CrossRef](#)]
20. Tesch, A.; Wenisch, C.; Herrmann, K.-H.; Reichenbach, J.R.; Warncke, P.; Fischer, D.; Müller, F.A. Luminomagnetic Eu³⁺- and Dy³⁺-doped hydroxyapatite for multimodal imaging. *Mater. Sci. Eng. C* **2017**, *81*, 422–431. [[CrossRef](#)]
21. Ashokan, A.; Menon, D.; Nair, S.; Koyakutty, M. A molecular receptor targeted, hydroxyapatite nanocrystal based multi-modal contrast agent. *Biomaterials* **2010**, *31*, 2606–2616. [[CrossRef](#)]
22. Xie, Y.; He, W.; Li, F.; Perera, T.S.H.; Gan, L.; Han, Y.; Wang, X.; Li, S.; Dai, H. Luminescence Enhanced Eu³⁺/Gd³⁺ Co-Doped Hydroxyapatite Nanocrystals as Imaging Agents In Vitro and In Vivo. *ACS Appl. Mater. Interfaces* **2016**, *8*, 10212–10219. [[CrossRef](#)] [[PubMed](#)]
23. Ignjatović, N.L.; Mančić, L.; Vuković, M.; Stojanović, Z.; Nikolić, M.G.; Škapin, S.; Jovanović, S.; Veselinović, L.; Uskoković, V.; Lazić, S.; et al. Rare-earth (Gd³⁺, Yb³⁺/Tm³⁺, Eu³⁺) co-doped hydroxyapatite as magnetic, up-conversion and down-conversion materials for multimodal imaging. *Sci. Rep.* **2019**, *9*, 16305. [[CrossRef](#)] [[PubMed](#)]
24. Zhang, C.; Lin, J. Defect-related luminescent materials: Synthesis, emission properties and applications. *Chem. Soc. Rev.* **2012**, *41*, 7938–7961. [[CrossRef](#)] [[PubMed](#)]
25. Cates, E.L.; Cho, M.; Kim, J.-H. Converting Visible Light into UVC: Microbial Inactivation by Pr³⁺-Activated Upconversion Materials. *Environ. Sci. Technol.* **2011**, *45*, 3680–3686. [[CrossRef](#)] [[PubMed](#)]
26. Salviulo, G.; Bettinelli, M.; Russo, U.; Speghini, A.; Nodari, L. Synthesis and structural characterization of Fe³⁺-doped calcium hydroxyapatites: Role of precursors and synthesis method. *J. Mater. Sci.* **2011**, *46*, 910–922. [[CrossRef](#)]
27. El Khouri, A.; Elaammani, M.; Della Ventura, G.; Sodo, A.; Rizzi, R.; Rossi, M.; Capitelli, F. Synthesis, structure refinement and vibrational spectroscopy of new rare-earth tricalcium phosphates Ca₉RE(PO₄)₇ (RE = La, Pr, Nd, Eu, Gd, Dy, Tm, Yb). *Ceram. Int.* **2017**, *43*, 15645–15653. [[CrossRef](#)]
28. Capitelli, F.; Rossi, M.; El Khouri, A.; Elaammani, M.; Corriero, N.; Sodo, A.; Della Ventura, G. Synthesis, structural model and vibrational spectroscopy of lutetium tricalcium phosphate Ca₉Lu(PO₄)₇. *J. Rare Earths* **2018**, *36*, 1162–1168. [[CrossRef](#)]
29. Altomare, A.; Rizzi, R.; Rossi, M.; El Khouri, A.E.; Elaammani, M.; Paterlini, V.; Della Ventura, G.; Capitelli, F. New Ca_{2.90}(Me²⁺)_{0.10}(PO₄)₂ β-tricalcium phosphates with Me²⁺ = Mn, Ni, Cu: Synthesis, crystal-chemistry, and luminescence properties. *Crystals* **2019**, *9*, 288. [[CrossRef](#)]

30. Baldassarre, F.; Altomare, A.; Corriero, N.; Mesto, E.; Lacalamita, M.; Bruno, G.; Sacchetti, A.; Dida, B.; Karaj, D.; Ventura, G.D.; et al. Crystal Chemistry and Luminescence Properties of Eu-Doped Polycrystalline Hydroxyapatite Synthesized by Chemical Precipitation at Room Temperature. *Crystals* **2020**, *10*, 250. [[CrossRef](#)]
31. Arkin, V.H.; Lakhera, M.; Manjubala, I.; Narendra Kumar, U. Solid state synthesis and characterization of calcium phosphate for biomedical application. *Int. J. Chem. Tech. Res.* **2015**, *8*, 264–267.
32. Rietveld, H.M. A profile refinement method for nuclear and magnetic structures. *J. Appl. Cryst.* **1969**, *2*, 65–71. [[CrossRef](#)]
33. Altomare, A.; Cuocci, C.; Giacovazzo, C.; Moliterni, A.; Rizzi, R.; Corriero, N.; Falcicchio, A. EXPO2013: A kit of tools for phasing crystal structures from powder data. *J. Appl. Cryst.* **2013**, *46*, 1231–1235. [[CrossRef](#)]
34. *Horiba Jobin Yvon DAS6 Fluorescence Decay Analysis Software User Guide, Version 2744.F*; HORIBA Horiba Scientific Inc.: Edison, NJ, USA, 2008; pp. 29–31.
35. Huang, S.; Zhu, J.; Zhou, K. Effects of Eu³⁺ ions on the morphology and luminescence properties of hydroxyapatite nanoparticles synthesized by one-step hydrothermal method. *Mater. Res. Bull.* **2012**, *47*, 24–28. [[CrossRef](#)]
36. Feng, Z.; Li, Y.; Huang, Y.; Seo, H.J. Luminescence properties of Eu²⁺ and Eu³⁺ doped calcium-deficient hydroxyapatite prepared in air. *J. Alloys Compd.* **2011**, *509*, 7087–7092. [[CrossRef](#)]
37. Li, Y.; Ooi, C.P.; Philip Hong Ning, C.; Aik Khor, K. Synthesis and characterization of neodymium (III) and gadolinium (III)-substituted hydroxyapatite as biomaterials. *Int. J. Appl. Ceram. Technol.* **2009**, *6*, 501–512. [[CrossRef](#)]
38. Altomare, A.; Campi, G.; Cuocci, C.; Eriksson, L.; Giacovazzo, C.; Moliterni, A.; Rizzi, R.; Werner, P.-E. Advances in powder diffraction pattern indexing: N-TREOR09. *J. Appl. Cryst.* **2009**, *42*, 768–775. [[CrossRef](#)]
39. Skorokhod, V.V.; Solonin, S.M.; Dubok, V.A.; Kolomiets, L.L.; Permyakova, T.V.; Shinkaruk, A.V. Decomposition activation of hydroxyapatite in contact with β -tricalcium phosphate. *Powder Metall. Metal. Ceram.* **2010**, *49*, 324–329. [[CrossRef](#)]
40. Landi, E.; Tampieri, A.; Celotti, G.; Sprio, S. Densification behaviour and mechanisms of synthetic hydroxyapatites. *J. Eur. Chem. Soc.* **2000**, *20*, 2377–2387. [[CrossRef](#)]
41. Zyman, Z.; Ivanov, I.; Rochmistrov, D.; Glushko, V.; Tkachenko, N.; Kijko, S. Sintering peculiarities for hydroxyapatite with different degrees of crystallinity. *J. Biomed. Mater. Res.* **2001**, *54*, 256–263. [[CrossRef](#)]
42. Garskaite, E.; Gross, K.-A.; Yang, S.-W.; Yang, T.C.-K.; Yang, J.-C.; Kareiva, A. Effect of processing conditions on the crystallinity and structure of carbonated calcium hydroxyapatite (CHAp). *CrystEngComm* **2014**, *16*, 3950–3959. [[CrossRef](#)]
43. Pogosova, M.A.; Eliseev, A.A.; Kazin, P.E.; Azarmi, F. Synthesis, structure, luminescence, and color features of the Eu- and Cu-doped calcium apatite. *Dye. Pigment.* **2017**, *141*, 209–216. [[CrossRef](#)]
44. Brown, I.D.; Altermatt, D. Bond-Valence Parameters Obtained from a Systematic Analysis of the Inorganic Crystal Structure Database. *Acta Crystallogr. B* **1985**, *41*, 244–247. [[CrossRef](#)]
45. *Inorganic Crystal Structure Database (ICSD), Version 2018-2*; Fachinformationszentrum: Karlsruhe, Germany, 2018.
46. Rossi, M.; Ghiara, M.R.; Chita, G.; Capitelli, F. Crystal-chemical and structural characterization of fluorapatites in ejecta from Somma-Vesuvius volcanic complex. *Am. Mineral.* **2011**, *96*, 1828–1837. [[CrossRef](#)]
47. Fleet, M.E.; Liu, X.; Pan, Y. Site preference of rare earth elements in hydroxyapatite [Ca₁₀(PO₄)₆(OH)₂]. *J. Solid State Chem.* **2000**, *149*, 391–398. [[CrossRef](#)]
48. Graeve, O.A.; Kanakala, R.; Madadi, A.; Williams, B.C.; Glass, K.C. Luminescence variations in hydroxyapatites doped with Eu²⁺ and Eu³⁺ ions. *Biomaterials* **2010**, *31*, 4259–4267. [[CrossRef](#)]
49. Low, H.R.; Phonthammachai, N.; Maignan, A.; Stewart, G.A.; Bastow, T.J.; Ma, L.L.; White, T.J. The crystal chemistry of ferric oxyhydroxyapatite. *Inorg. Chem.* **2008**, *47*, 11774–11782. [[CrossRef](#)]
50. Harcharras, M.; Ennaciri, A.; Capitelli, F.; Mattei, G. Vibrational spectra and thermal dehydration of Co₂P₂O₇·6H₂O diphosphate. *Vib. Spectrosc.* **2003**, *33*, 189–196. [[CrossRef](#)]
51. Kim, J.H.; Kim, S.H.; Kim, H.K.; Akaike, T.; Kim, S.C. Synthesis and characterization of hydroxyapatite crystals: A review study on the analytical methods. *J. Biomed. Mater. Res.* **2002**, *62*, 600–612.
52. Berzina-Cimdina, L.; Borodajenko, N. Research of Calcium Phosphates Using Fourier Transform Infrared Spectroscopy. In *Infrared Spectroscopy Materials Science, Engineering and Technology*; Theophanides, T., Ed.; IntechOpen: London, UK, 2012. [[CrossRef](#)]

53. Constantin, L.V.; Iconaru, S.; Ciobanu, C.S. Europium doped hydroxyapatite for applications in environmental field. *Rom. Rep. Phys.* **2012**, *64*, 788–794.
54. Rizzi, R.; Capitelli, F.; Della Ventura, G.; Hami, W.; Corriero, N.; Rossi, M.; Altomare, A. Preparation, structural and spectroscopical properties of silver terbium diphosphate AgTbP_2O_7 . *Z. Für Krist. Cryst. Mater.* **2019**, *234*, 363–369. [[CrossRef](#)]
55. El Khouri, A.; Zegzouti, A.; Elaatmani, M.; Capitelli, F. Bismuth-substituted hydroxyapatite ceramics synthesis: Morphological, structural, vibrational and dielectric properties. *Inorg. Chem. Commun.* **2019**, *110*, 107568. [[CrossRef](#)]
56. Fowler, B.O. Infrared studies of apatites. I. Vibrational assignments for calcium, strontium, and barium hydroxyapatites utilizing isotopic substitution. *Inorg. Chem.* **1974**, *13*, 194–207. [[CrossRef](#)]
57. Predoi, D.; Barsan, M.; Andronescu, E.; Vatasescu-Balcan, R.A.; Costache, M. Hydroxyapatite-iron oxide bioceramic prepared using nano-size powders. *J. Optoelectron. Adv. Mater.* **2007**, *9*, 3609–3613.
58. Get'man, E.I.; Loboda, S.N.; Tkachenko, T.V.; Yablochkova, N.V.; Chebyshev, K.A. Isomorphous substitution of samarium and gadolinium for calcium in hydroxyapatite structure. *Russ. J. Inorg. Chem.* **2010**, *55*, 333–338. [[CrossRef](#)]
59. Markovic, M.; Fowler, B.O.; Tung, M.S. Preparation and comprehensive characterization of a calcium hydroxyapatite reference material. *J. Res. Natl. Inst. Stand. Technol.* **2004**, *109*, 553–568. [[CrossRef](#)] [[PubMed](#)]
60. Jastrzbski, W.; Sitarz, M.; Rokita, M.; Bułat, K. Infrared spectroscopy of different phosphates structures. *Spectrochim. Acta A* **2011**, *79*, 722–727. [[CrossRef](#)] [[PubMed](#)]
61. Blasse, G. Influence of local charge compensation on site occupation and luminescence of apatites. *J. Solid State Chem.* **1975**, *14*, 181–184. [[CrossRef](#)]
62. Peacock, R.D. The Intensities of Lanthanide $f \leftrightarrow f$ Transitions. *Struct. Bond.* **1975**, *22*, 83–122.
63. Wachtler, M.; Speghini, A.; Gatterer, K.; Fritzer, H.P.; Ajo, D.; Bettinelli, M. Optical Properties of Rare-Earth Ions in Lead Germanate Glasses. *J. Am. Ceram. Soc.* **1998**, *81*, 2045–2052. [[CrossRef](#)]
64. Han, Y.; Wang, X.; Dai, H.; Li, S. Synthesis and luminescence of Eu^{3+} doped hydroxyapatite nanocrystallines: Effects of calcinations and Eu^{3+} content. *J. Lumin.* **2013**, *135*, 281–287. [[CrossRef](#)]
65. Prichodko, A.; Enrichi, F.; Stankeviciute, Z.; Benedetti, A.; Grigoraviciute-Puroniene, I.; Kareiva, A. Study of Eu^{3+} and Tm^{3+} substitution effects in sol-gel fabricated calcium hydroxyapatite. *J. Sol-Gel Sci. Technol.* **2017**, *81*, 261–267. [[CrossRef](#)]
66. Ternane, R.; Trabelsi-Ayedi, M.; Kbir-Arighuib, N.; Piriou, B. Luminescent properties of Eu^{3+} in calcium hydroxyapatite. *J. Lumin.* **1999**, *81*, 165–170. [[CrossRef](#)]
67. Piriou, B.; Fahmi, D.; Dexpert-Ghys, J.; Taitai, A.; Lacout, J.L. Unusual fluorescent properties of Eu^{3+} in oxyapatites. *J. Lumin.* **1987**, *39*, 97–103. [[CrossRef](#)]
68. Brixner, L.H.; Crawford, M.K.; Blasse, G. Optical luminescence of electronic and vibronic transitions in $\text{Gd}_{2-x}\text{Y}_x(\text{SO}_4)_3 \cdot 8\text{H}_2\text{O}$. *J. Solid State Chem.* **1990**, *85*, 1–7. [[CrossRef](#)]
69. Blasse, G.; Brixner, L.H.; Mroczkowski, S. The electronic and vibronic transitions in the emission spectrum of Gd^{3+} in the yttrium hydroxide structure. *J. Solid State Chem.* **1989**, *82*, 303–306. [[CrossRef](#)]
70. Blasse, G.; Dirksen, G.J. Luminescence of $\text{Eu}(\text{III})$ in $(\text{NH}_4)_3\text{YCl}_6$: Nonradiative transitions induced by the second coordination sphere. *J. Solid State Chem.* **1992**, *96*, 258–262. [[CrossRef](#)]
71. Blasse, G.; Meijerink, A.; de Mello Donegà, C. Vibronic rare earth spectroscopy: Results and pitfalls. *J. Alloys Compd.* **1995**, *225*, 24–27. [[CrossRef](#)]
72. Blasse, G. Vibronic transitions in rare earth spectroscopy. *Int. Rev. Phys. Chem.* **1992**, *11*, 71–100. [[CrossRef](#)]
73. Hou, D.; Liang, H.; Xie, M.; Ding, X.; Zhong, J.; Su, Q.; Tao, Y.; Huang, Y.; Gao, Z. Bright green-emitting, energy transfer and quantum cutting of $\text{Ba}_3\text{Ln}(\text{PO}_4)_3: \text{Tb}^{3+}$ ($\text{Ln} = \text{La}, \text{Gd}$) under VUV-UV excitation. *Opt. Express* **2011**, *19*, 11071–11083. [[CrossRef](#)]

